Magnet Positioner

Dragoș Ileana, Nian Tian Lin, Qu Tianchen and Badr Zouggari

October 31, 2025

Abstract

With the continuous scaling of semiconductor qubit architecture, the need for more space within the dilution refrigerator becomes critical, as required by the ever increasing amount of wiring and electronics inside. In this context, the superconducting magnet inside the refrigerator can become a major bottleneck, occupying valuable space inside the dilution refrigerator. Here, we present the design and development of a permanent magnet positioner outside of the the fridge to fully replace the superconducting solenoid currently being used by the Veldhorst group at QuTech. The system was modelled and manufactured considering several success criteria. To study the effect of the magnetic field at the device location, we performed simulations of the field strength around the magnet and compared them with field measurements in a single direction. Although the assembly was not completed on time, this design still shows a promising approach at addressing future scalability concerns.

1 Introduction

1.1 Theory

Semiconductor spin qubits represent one of the early studied types of qubits, providing a natural two-level system, wherein a qubit is encoded in the state of a single spin 1/2 electron/hole confined in a semiconductor quantum dot [1], [2]. The small, nanometric size (~ 100 nm) of quantum dots provides the benefit of dense integration of many qubits on a small quantum device [2], [3]. This is an important requirement for the realization of large-scale, fault-tolerant quantum computing, as well as for relevant applications in cryptography, all of which necessitate a large number of physical qubits (more than 10^6) [4], [5]. Additionally, manufacturing and scaling of semiconductor devices for spin qubits is facilitated by their similarity and compatibility with classical semiconductor devices (i.e., transistors) [3], [6]. One downside is that the complexity of circuitry needed to address qubits in such quantum processors increases fast with larger number of qubits, thus limiting the maximum number of quantum dots on such devices [2], [3].

Gallium-Arsenide (GaAs) for electron spin qubit devices emerged as a first promising platform for the realization of spin qubits. GaAs provided a sparse 2D electron gas (2DEG) and allowed to isolate few (or single) electrons into a 0D space. More recently, Germanium (Ge) hole spin qubit devices have also been employed, thanks to suppressed noise from hyperfine interactions when compared to GaAs, resulting in longer coherence times [6]. The limited hyperfine interactions in Ge stem from the low abundance of nonzero nuclear spins in the environment (with the possibility of further isotopic enrichment), but also from the p-type character of the valence band [6].

An important characteristic of Ge qubits is the strong natural spin-orbit coupling which acts as a double-edged sword. On one hand, it enables all-electrical control of qubits and fast gates through electron-dipole spin resonance (EDSR). This way, shorter gate times are achieved when compared to coherence times [7]. Moreover, no other microstructures (e.g., nanomagnets) are used to control the spin, as in the case of electron spin qubits [6].

On the other hand, strong spin-charge coupling and dependence of g factors on the applied electric field imply that charge noise becomes a major nuisance for hole-spin coherence [6]. Nevertheless, it is still possible to find "sweet spots" in qubit operation such that hole-spins are not affected by charge noise. The g-tensor features strong anisotropy, meaning that the out-of-plane and in-plane components ($g_\perp$ and $g_\parallel$, respectively) differ greatly ($|g_\perp| \gg |g_\parallel|$) [6]. As most Ge devices require a strong magnetic field $\mathbf{B}$, even small deviations of $\mathbf{B}$ from the g-tensor plane can greatly affect qubit properties, resulting in different quantization axes of qubits [8].

Furthermore, the hyperfine couplings become negligible when **B** is in-plane, due to the Ising characteristic of hyperfine interactions [8]. Hence, limiting hyperfine interactions requires finding a second "sweet-spot" in **B** field alignment, but this time with respect to the hyperfine plane.

Finding an optima such that **B** is aligned to both of the g-tensor and hyperfine interactions[1] planes can be hard and sensitive to small angle variations of **B** [6], [8], and might necessitate striking a balance between the two. In this context, changing the orientation of **B** appears as the natural solution.

1.2 Problem context

The Veldhorst research group at QuTech currently operates Ge hole-spin qubit experiments by using a superconducting solenoid to generate the uniaxial magnetic field **B** necessary for qubit control [9]. Specifically, the solenoid is a 3-0-0 Tesla (T) magnet, meaning it can create up to 3 T on a single axis, with a bore of 200 mm ($\sim$ 190 mm sample space) supplied by Bluefors. The uniaxial nature of **B** prompted the group to install an additional gantry system for moving a permanent magnet outside the dilution refrigerator [9]. This permanent magnet is used to fine-tune the magnetic field at the qubit location, thereby solving one of the limitations of the solenoid. The experiment utilized a Ge/SiGe heterostructure processor, with 10 qubits arranged in a 2D array [7]; see figure 1. Superconducting vector magnets were proposed as an alternative solution[10], but were deemed unfeasible due to higher space and heat load considerations [9].
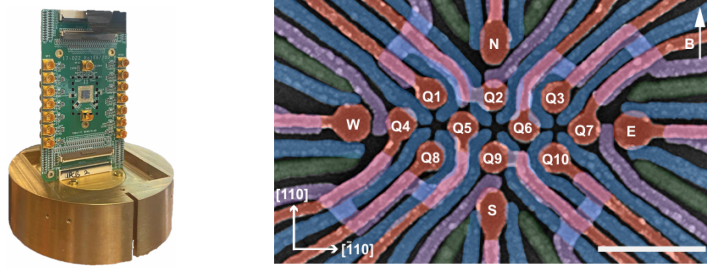

Figure 1: *The 10 qubit physical processor (left) and its qubit layout used to test the external magnet positioner [7], [9].*

While this configuration functions effectively for small-scale demonstrations with approximately 10 qubits, it presents an obstacle for the planned transition to the 1000 quantum dot project, where every bit of space inside the fridge is valuable. A successful demonstration of qubit control with the superconducting solenoid turned off and only using the permanent magnet underscores the possibility to remove the solenoid entirely [9].

A successful resolution of this challenge can have a positive impact on the scalability of semiconductor spin qubits. The dilution refrigerator's interior represents a fixed, finite resource. However, superconducting magnets, while providing excellent field control, consume critical volume that could otherwise house cryogenic control electronics, signal conditioning components, and extensive wiring necessary for operating hundreds or thousands of qubits. Recent demonstrations have shown that room-temperature permanent magnets positioned external to the cryostat can achieve comparable qubit performance metrics, including dephasing times $T_2^* = 13$ μs and gate fidelities exceeding 99.9% [9]. This breakthrough suggests that relocating the magnetic field source outside the refrigerator is technically feasible and could unlock the spatial capacity required for qubit scale-up.

2 Problem statement, scope, and success criteria

2.1 The Core Challenge: space limitations in scaled qubit systems

Each qubit in semiconductor quantum processors uses dedicated wiring for control and readout operations. As the qubit count increases proportionally, so does the demand for coaxial lines, DC

---

[1]It is worth noting that isotopic enrichment can remove hyperfine couplings and thus simplify this problem, to the extent that the optima for the g-tensor in-plane alignment of **B** dominates [8].

connections, and cryogenic electronics housed within the dilution refrigerator. The superconducting solenoid currently occupies valuable space inside the cryostat, space that must be reclaimed to accommodate the extensive circuitry required for 1000 quantum dots. Without addressing this constraint, the integration of necessary control infrastructure becomes physically impossible, effectively halting scalability efforts.

Therefore, the problem statement can be summarized as follows:

To enable scaling quantum processors from tens to thousands of qubits, an improved magnet positioning system must be designed to replace the bulky superconducting solenoid inside the dilution refrigerator, reclaiming essential space for expanded wiring and electronics.

2.2 Magnetic field alignment requirements

Germanium hole spin qubits exhibit strong spin-orbit interaction, which enables high-fidelity quantum gates but simultaneously creates a pronounced dependence on magnetic field orientation [9]. Precise alignment of the magnetic field to the sample plane is essential to minimize dephasing from hyperfine interactions and maximize spin control fidelity [9]. Current experiments using superconducting solenoid magnets achieve single-qubit Clifford gate fidelities above 99.9% [9]. Any alternative magnetic field solution must maintain this level of precision while simultaneously addressing the space constraints.

2.3 Scope of the project

In this section, the initial scope of the project is discussed. This scope was established following discussions between the team had and the project supervisor, wherein different technical challenges and initial solutions were pointed out, as outlined below. This project focuses on adapting an existing prototype magnet positioner system to the ProteoxMX dilution refrigerator in QuTech's laboratory.

2.3.1 Technical challenges

- **Adapting New Fridge Layout:** Previously, the magnet positioner was designed for a smaller Bluefors cryogenic fridge with a different layout. In order to utilize a magnet positioner for the new ProteoxMX fridge, a new adapted frame is needed. At the same time, aiming for component reusability across the two design is desired.

- **Cryogenic Temperature Effects:** The Meissner effect in superconducting materials within the refrigerator can distort magnetic field distributions at different temperature stages. Understanding these temperature-dependent field modifications could be very helpful for maintaining consistent qubit operation.

- **Mechanical Vibration Control:** Eddy currents induced in conductive materials by moving permanent magnets can generate vibrations that propagate through the refrigerator structure. These vibrations translate to magnetic field fluctuations at the qubit location, directly degrading coherence times [11]. The project could incorporate some sort of damping mechanism to attenuate vibrations and improve overall system stability.

- **Precision Positioning:** Achieving 0.1 mm positioning accuracy requires careful attention to motor selection, control algorithms, and mechanical transmission systems. The implementation will explore servo-motor upgrades and gear systems between motors and leadscrews to enhance positioning precision.

- **Safety Considerations:** Strong permanent magnets present hazards during operation and failure scenarios. The design should include physical stops to catch the carriage in case of mechanical failure and non-magnetic rails for z-axis movement to prevent unwanted magnetic interactions.

Certain aspects lie beyond the current project scope. The design and fabrication of the qubit samples themselves, while connected to the magnet system performance, remain separate efforts. Additionally, the project focuses on the ProteoxMX [12] system; while insights may inform future adaptations to other refrigerator models, explicit multi-system compatibility is not a primary objective.

2.4 Success Criteria

2.4.1 Quantitative performance targets

- **Positioning Precision:** Motor control systems must achieve positioning accuracy of at least 0.1 mm in all three axes (X, Y, Z). This tolerance ensures that magnetic field variations due to positional uncertainty remain negligible compared to the qubit's field sensitivity.

- **Magnetic Field Range and Control:** The system must generate magnetic fields continuously adjustable up to 25 mT at the sample location.

- **Qubit Performance Preservation:** The adapted magnet positioner must enable qubit dephasing times T_2^* at least equal to current performance with the superconducting solenoid.

- **Gate Fidelity Maintenance:** Single-qubit gate fidelities of $\geq 99.9\%$ must be achieved in benchmarking tests using the external magnet system.

2.4.2 Functional requirements

- **Magnetic Field Mapping Capability:** The system must enable comprehensive characterization of the magnetic field distribution around the sample location.

- **Structural Stability:** The mechanical structure must exhibit sufficient rigidity to minimize vibration-induced magnetic field fluctuations.

2.5 Approach and implementation strategy

The project leverages a proven concept—the gantry-style permanent magnet positioner demonstrated in recent germanium qubit experiments [9]. This approach positions a room-temperature permanent magnet on a three-axis positioning system located beneath the dilution refrigerator. By maintaining the magnet external to the cryostat, the entire volume previously occupied by the superconducting solenoid becomes available for qubit sample infrastructure [9].

2.5.1 Advantages of the external permanent magnet approach

- Eliminates the need for bulky superconducting coils and associated infrastructure inside the cryostat, freeing space for qubit wiring and electronics [9].

- Permanent magnets require no electrical power during operation, removing a heat load source from the cryogenic environment [11].

- Comparable or superior qubit coherence times relative to superconducting solenoids, possibly due to reduced magnetic field noise [11].

- Allows in-situ adjustment of field strength and orientation without warming the refrigerator or disrupting experiments [9].

2.5.2 Trade-offs and limitations

- Permanent magnets generate fixed intrinsic field strengths, making continuous field adjustment more complex [9].

- Positioning mechanism introduces moving parts, creating potential vibration sources that require active damping.

- Strong permanent magnets necessitate proper shielding, mechanical stops, and careful handling.

Alternative approaches considered include hybrid systems and Halbach arrays, but the gantry-style positioning system offers the most direct path to reclaiming cryostat space while maintaining the required field control for high-fidelity qubit operations [9].

3 Methods and approaches

The following section will include the various steps and approaches taken to produce the magnet positioner assembly as shown in Fig. 2. The assembly is largely based on the design created by Yu et al. [9], which are improved upon to accommodate for a larger fridge and stronger magnet. The assembly was made using Autodesk Inventor, a CAD software used for 3D mechanical design and simulation. The system can be separated into a stationary part called the gantry frame and a movable part categorized as the xyz-assembly.

3.1 xyz movement

The movement of the magnet makes use of four NEMA 17 stepper motors with a maximum holding torque of 0.55 Nm. This choice is inspired by the way 3D printers and CNC machines operate, which enables motion on the three axes of the Cartesian coordinate system.

Using a lead screw with a 8 mm diameter and 2 mm pitch, this translates into a maximum load of ~ 36 kg per motor, where we show the calculation in Appendix A. However, to account for the fact that the moving torque will be less than the holding torque and to allow for a margin of error, each motor should not exceed 50% of the maximum load (i.e. 18 kg per motor).

The motors are controlled with a CNC shield V3 connected to an arduino UNO board. This enables movement of three motors for all three axes with a fourth motor that can be synchronized on any axis. In this case, two motors are used to move the z direction and the remaining two move the x and y directions respectively.

To improve the positioning precision mentioned in Section 2.4.1, we have replaced the original lead screw trapezoidal nuts in the x and y directions with spring loaded anti-backlash nuts. This adds tension on the screw from both directions and prevents any unwanted motion caused by loose fitting between the two parts. A similar replacement in the z direction is not necessary, since gravity acts as a 'natural' anti-backlash mechanism already.

We include several SBR16 linear rails to support and guide the movement of the motors along the y and z directions. An MGN12H slider is used for the x direction.

3.2 Material choices

An important step in the design is to select the best materials for each part, which are influenced by several factors listed below:

- **Weight**: The xyz assembly in particular requires special attention due to the motors having a weight limitation as shown in Section 3.1.

- **Magnetic properties**: Since we work with a strong magnet, it is important to consider non-magnetic materials for safety but also to not influence the magnetic field created by the magnet.

- **Rigidity**: Depending on the functionality of the component, rigidity might have a higher or lower priority. Critical parts that are important for structural support require high rigidity to be able to hold up the frames above. In contrast, a stepper motor bracket can have low rigidity.

Considering the above factors, our choice of materials narrows down to three different kinds: stainless steel, PLA[2] filament and aluminium alloy.

While stainless steel has a high density, it offers high rigidity in return. This makes it a good option for small components that are important for stability of the entire system. For example, the z plate brackets are crucial components to connect the xyz assembly with the gantry frame. These parts are small, but have to support a lot of weight.

PLA is very lightweight with low durability and parts made from it can be easily done by a 3D printer. Any parts that hold something small in place and are not needed for the structure of the

---

[2]PLA is polylactic acid, the plastic filament used for 3D printing.

system, will be created from this material.

Aluminium alloy has a roughly three times lower density compared to stainless steel while still offering good rigidity, although not as high as stainless steel. Therefore, any large piece that will heavily impact the total weight of the assembly can be made from aluminium alloy.
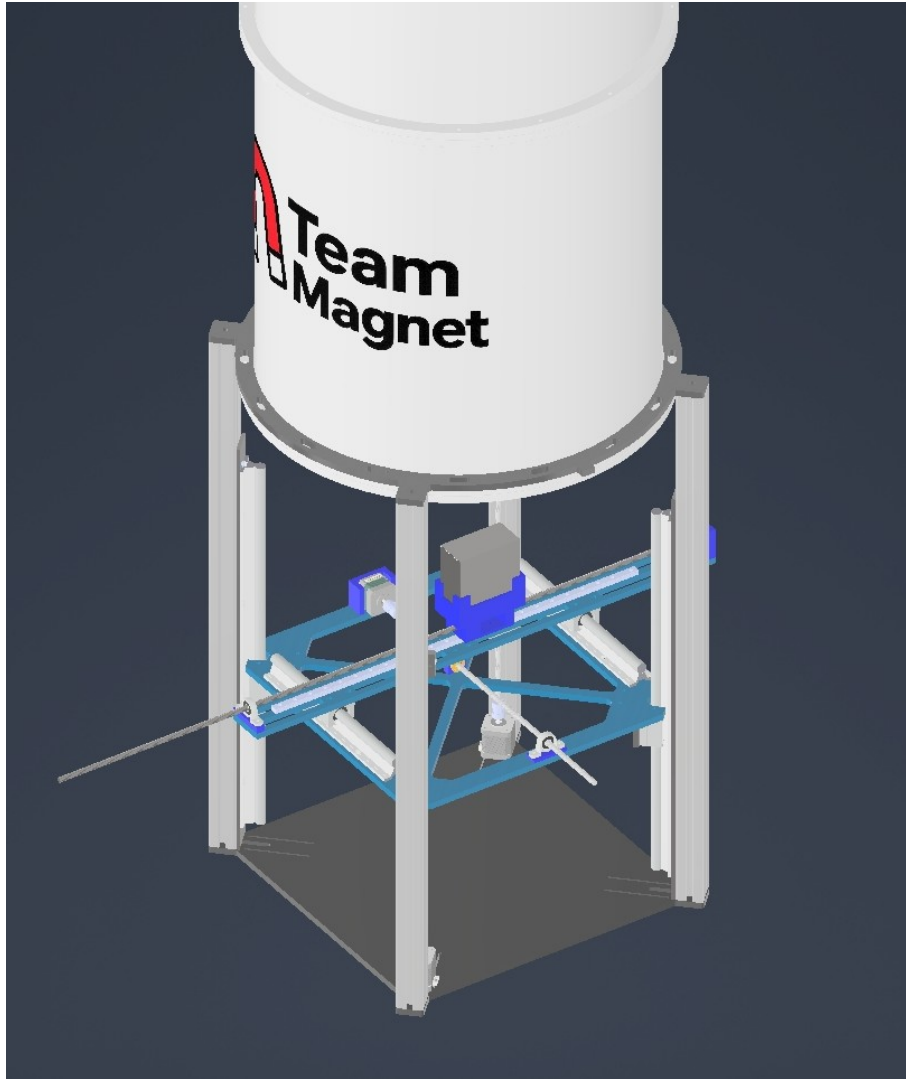

Figure 2: Full magnet positioner assembly attached to a cylindrical dilution refrigerator.

3.3 Gantry frame

Fig. 3 shows the gantry frame, which is the static outer frame of the system. The half rings and base plate are made from aluminium alloy while any brackets for vertical movement are created using stainless steel.

At the top, a ring shape is used to fit with and rest onto the rim of the dilution fridge. Compared to the smaller fridge from Ref. [9], the ProteoxMX fridge has 8 equidistant bolts protruding from the rim with 3 additional bolts appearing irregularly on halfway points between some of the regularly spaced bolts. To account for the 11 extra bolts, we have decided to create 16 holes spaced evenly (at every 22.5 degrees) around the ring. This allows for some amount of freedom to place the magnet positioner in the desired orientation. Notably, the holes themselves are designed large enough to enable up to 4 degrees of movement.

The base plate on the bottom, aside from the increased size, remains largely the same. A small modification is the addition of slotted holes in the corners of the base plate. This allows the base plate to be compatible with multiple fridge sizes, potentially future-proofing this design.
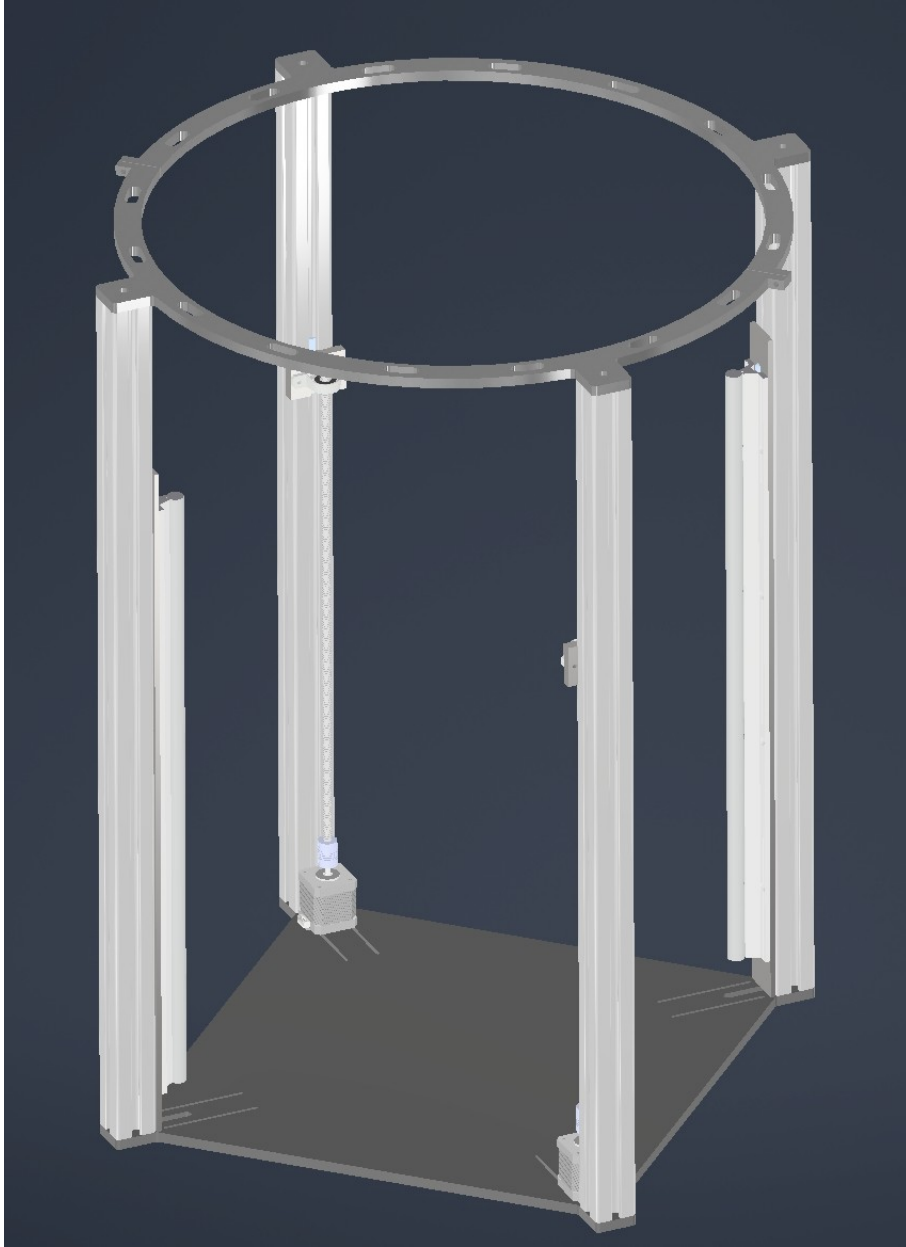
Figure 3: Gantry frame of the magnet positioner. The main components consist of three parts. Two half rings are created to rest on the bottom rim of the fridge, the z translation parts enable vertical movement and the base plate connects the four pillars to create a stable base.

3.4 xyz-assembly

Fig. 4 shows the assembly that is able to move on the z axis using the motors and rails connected to the gantry frame. Fig. 5 is mounted on top and can be moved in the y direction. Finally, the magnet itself can be moved on the guide rail in the x direction.

All of the parts indicated with dark blue and purple are not integral to the structural stability and are therefore 3D printed. The pillow block bearings and motors are mounted on top of brackets to make sure they are aligned with each other.

The plates indicated with light blue are made from aluminium alloy. The triangle shaped cutouts in Fig. 4 are added to reduce the weight of the plate without strongly impacting the structural integrity of the component. Similarly, the plate in Fig. 5 rectangular cutouts.

Before starting the manufacturing procedure of the parts, we inferred the entire weight of the xyz assembly from the CAD files. This showed that the xyz assembly totaled around 13 kg, staying well within the margin that two motors can handle in the z direction.
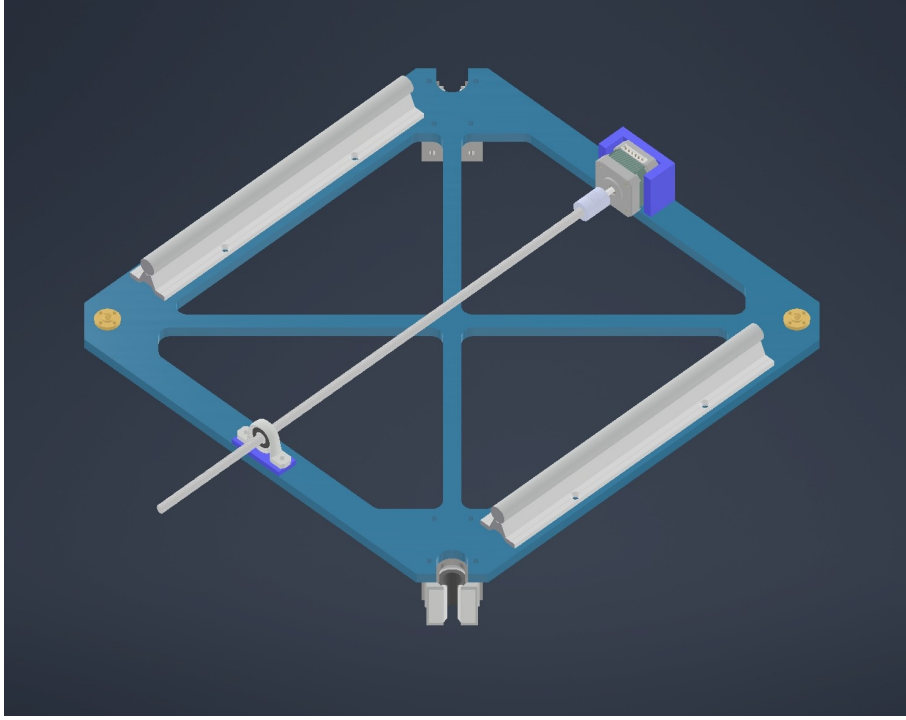
Figure 4: Diagram showing the movable frame of the magnet positioner in the z direction
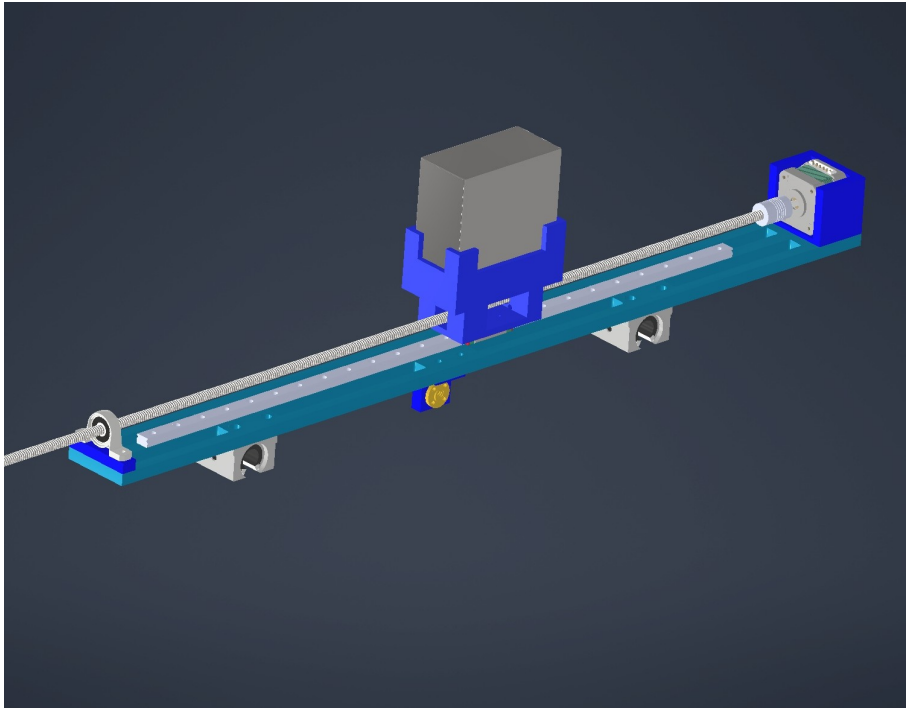

Figure 5: Diagram showing the movable frame of the magnet positioner in the y direction. Additionally, the magnet holder itself is movable in the x direction

4   Results

Our results pertain mostly to measurements of the magnetic field as its x-axis position is varied. Due to an unexpected delay in the plate fabrication, we were not able to assemble the whole magnet positioner by the time this report is written. However, we are able to theoretically analyse the magnet performance and, with the help of simulation, verify the viability of the approach.

4.1 Magnetic field at different distances

We measure the field strength with a 3D Hall sensor[3]. The measurement setup can be seen in Fig. 6 where we move the sensor perpendicular from the centre of the magnet. We log the measurement data using evaluation software developed by Infineon Technologies that is compatible with the Hall sensor. The resulting mean field strength can be seen in Fig. 8. Here, we also compare it to the simulation using Magpylib [13][14]. This helps us verify the correctness of our simulation. The simulation is normalized by setting the magnetic field strength to be equal to the measurement result for a distance of 7cm.

The simulation of overall magnetic field in the x-y plane can be seen in Fig. 7.

Figure 6: The sensor is at the centre of the magnet. Here, we move the magnet instead of the sensor. This specific instance has a 7cm distance. The red and green colour on the magnet shows its magnetisation direction and the coordinate arrows show the sensor location. The blue dotted line shows the movement for adjusting distance.
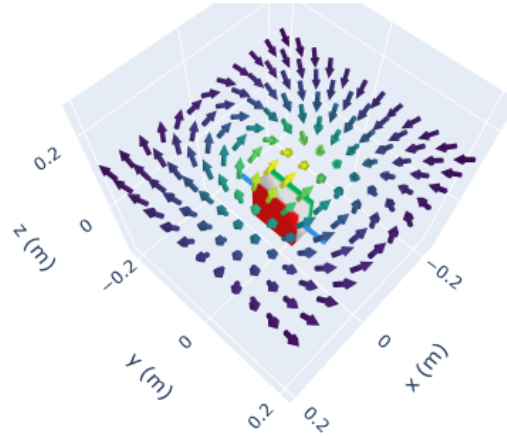

Figure 7: Since the magnetic field reaches the target 25mT in practice when 7cm away from the magnet surface, we show here the field distribution with z=7cm

---

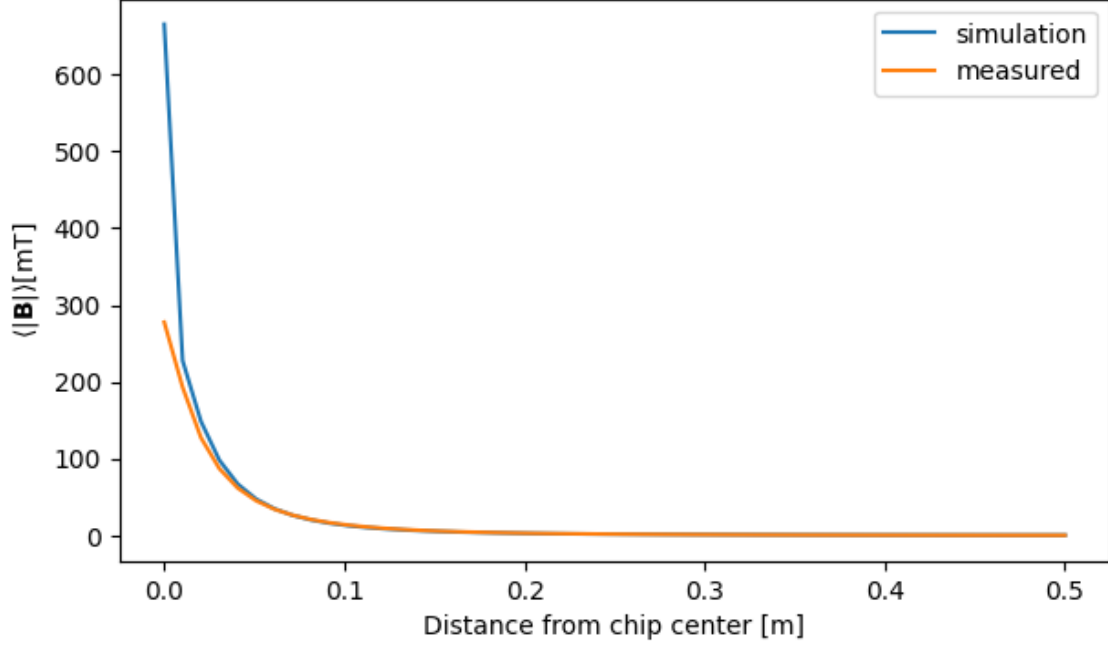[3]Model TLE493DW2B6MS2GOTOBO1 from Infineon Technologies

Figure 8: The mean field amplitude when chip is at different distances from the magnet.

4.2 Inhomogeneity of the magnetic field

The size of a quantum dot is at nanometer scale; therefore, although the magnetic field provided by the external permanent magnet is far from uniform, a chip with few quantum dots still experiences a close to uniform field. However, this could be a concern as one scales up the number of quantum dots on a single chip. In the Veldhorst lab, people are interested in making a 1000 quantum dot chip, with a $10 * 100$ square layout, where the distance between each adjacent dot is 200nm, making the quantum dots take a $20\mu m * 2\mu m$ area. For simplicity, we assume the chip to be a $20\mu m * 20\mu m$ square. This raises the question how much influence the inhomogeneity of the magnetic field will have on the future 1000 quantum dot chip.

To address this, we introduce a new quantity called deviation. For all possible magnetic field values on the chip $\{\mathbf{B}_i\}$, the deviation d is

$$d = \max_{\mathbf{r},\mathbf{r}' \text{ in chip}} \frac{||\mathbf{B}(\mathbf{r}) - \mathbf{B}(\mathbf{r}')||_2}{||\mathbf{B}_{\text{chip}}||_2}. \tag{1}$$

Which represents the maximum vector difference relative to the mean amplitude of the field across the chip.

This deviation can be estimated theoretically with the dipole moment approximation. Assuming that the magnet has a dipole moment $\mathbf{m}$ we can recall that the magnetic field can be approximated as:

$$\mathbf{B}(\mathbf{r}) = \frac{\mu_0}{4\pi} \left[\frac{3\mathbf{r}(\mathbf{m} \cdot \mathbf{r})}{r^5} - \frac{\mathbf{m}}{r^3} \right] \tag{2}$$

We switch to the spherical coordinate where magnetic moment $\mathbf{m}$ is pointing at the positive direction of the z-axis

$$\mathbf{B}(r, \theta, \phi) = \frac{\mu_0}{4\pi} \left[\frac{3|\mathbf{m}|\cos\theta}{r^3}\hat{r} - \frac{\mathbf{m}}{r^3} \right] \tag{3}$$

.

Since we are already using dipole approximation, we are only interested in the first order effect

of the field, which is captured by the gradient $\nabla \mathbf{B}$:

$$\frac{\partial \mathbf{B}}{\partial r} = \frac{-3\mu_0}{4\pi} \left[\frac{3|\mathbf{m}|\cos\theta}{r^4}\hat{r} - \frac{\mathbf{m}}{r^4} \right] \tag{4}$$

$$= \frac{-3\mathbf{B}}{r} \tag{5}$$

$$\frac{\partial \mathbf{B}}{\partial \theta} = -\frac{\mu_0}{4\pi}\frac{3|\mathbf{m}|\sin\theta}{r^3}\hat{r} \tag{6}$$

$$\frac{\partial \mathbf{B}}{\partial \phi} = 0 \tag{7}$$

The deviation can be first-order approximated as

$$d = \max_{\mathbf{a}\in\{0\}\times[0,a]\times[0,a]} \frac{||\mathbf{a}\cdot\nabla\mathbf{B}||_2}{||\mathbf{B}||_2} \tag{8}$$

where $\mathbf{a}$ is some relative position within the chip with width a.

Since we want in-plane magnetic field, the chip position will be perpendicular to the moment $\mathbf{m}\cdot\mathbf{r} = 0$ or $\theta = \frac{\pi}{2}$ and thus the first term in dipole magnetic field expression vanish, thus

$$\frac{\partial \mathbf{B}}{\partial \theta}\bigg|_{\mathbf{m}\cdot\mathbf{r}=0} = -3||\mathbf{B}||_2\hat{r}. \tag{9}$$

Thus if we express the gradient in normalized $\hat{r}, \hat{\theta}, \hat{\phi}$ basis

$$\frac{\nabla\mathbf{B}}{||\mathbf{B}||_2}\bigg|_{\theta=\frac{\pi}{2}} = \begin{bmatrix} \frac{3}{r}\hat{\theta} & -\frac{3}{r}\hat{r} & 0 \end{bmatrix} \tag{10}$$

We see that the deviation will have the same $\frac{3}{r}$ decay in the $\hat{r}$ or $\hat{\theta}$ direction, but it will vanish in the $\hat{\phi}$ direction. Since our chip is in $\hat{\theta} - \hat{\phi}$ plane, the deviation is

$$d = \frac{3a}{r} \tag{11}$$

Deviation with other chip orientations can also be derived from (10).

In order to cross-check whether the dipole approximation fits our case, we also perform a simulation. Here, we assume that permeability is constant and the magnet has uniform magnetisation.

To evaluate the magnetic field gradient, we use the same setup as the previous subsection as seen in Fig. 6.

We collect samples $\{\mathbf{B}_i\}$ of the magnetic field from 400 evenly spaced locations in the $20\mu m \times 20\mu m$ chip and the deviation estimator becomes:

$$d = \max_{i,j} \frac{||\mathbf{B}_i - \mathbf{B}_j||_2}{\langle ||\mathbf{B}||_2 \rangle}.$$

Note that deviation as a relative quantity is independent of the magnetisation strength of the actual magnet.
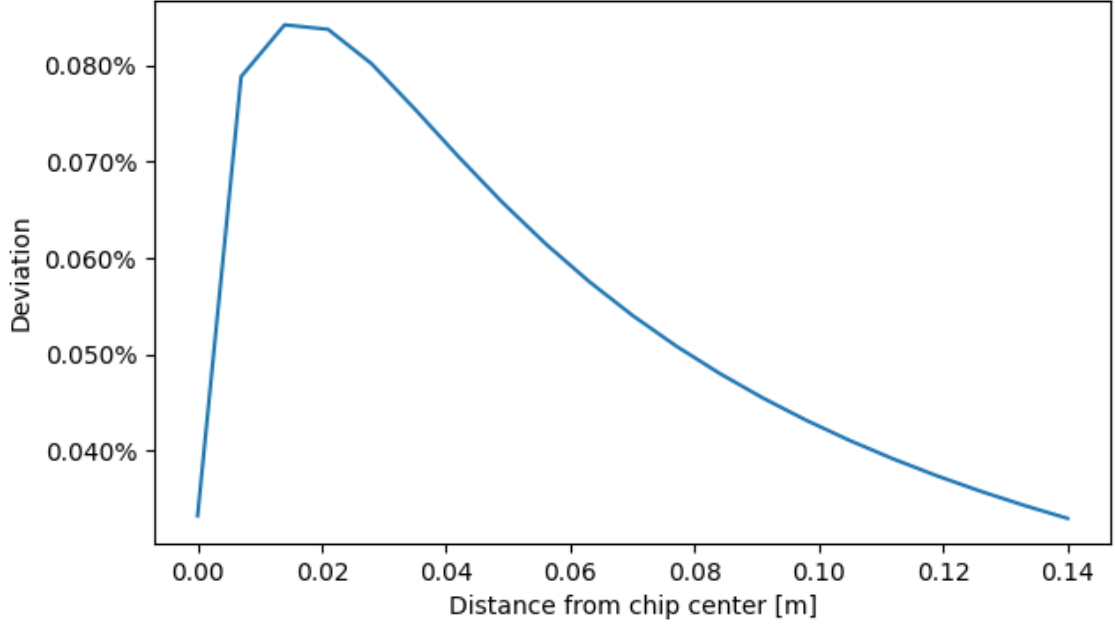
Figure 9: The deviation when chip is at different distances from the magnet.
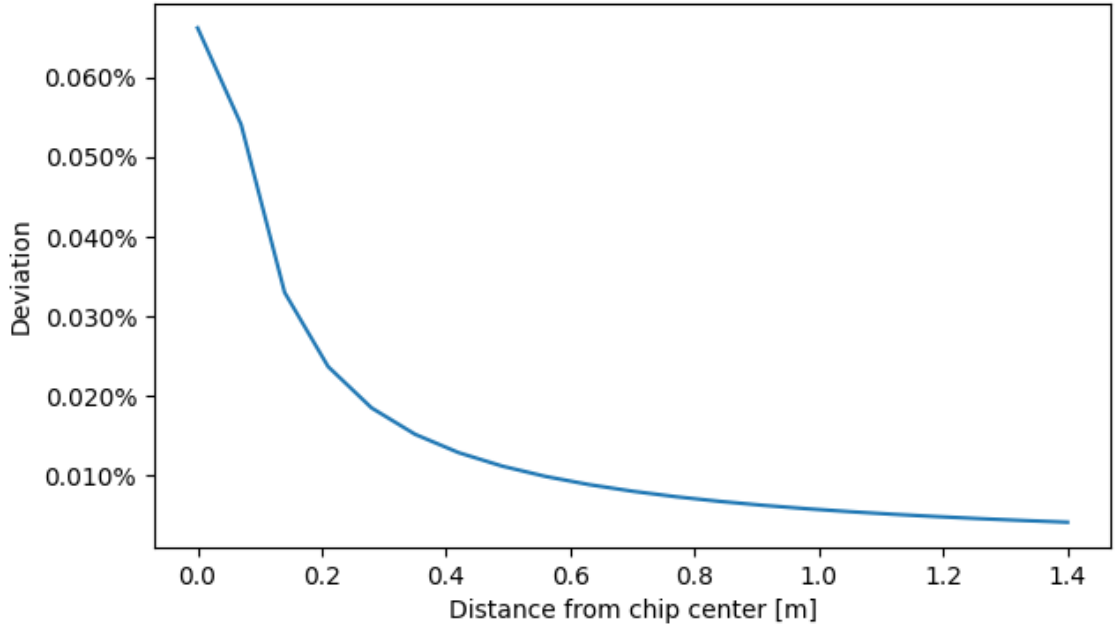

Figure 10: We see full dipole approximation regime for $z > 0.2$m.

From the simulation results in Fig. 9,10, we can see that the magnetic deviation is more than three orders of magnitude lower than the mean magnetic field. Since in fabrication it is common to have the g-factor vary by a factor of 2 across different quantum dots [15], the magnetic field gradient will not be the dominating term for qubit frequency fluctuations.

We also see that deviation decreases as expected from our theoretical report except when the distance is very close. This is expected since the dipole approximation breaks down in close range. Instead, we see a sharp increase from zero. Low deviation for a close chip is largely due to the magnetic field being almost uniform near its surface. Thus we have a peak deviation between uniform approximation regime and dipolar approximation regime.

We may also be interested in how the deviation depends, on the orientation of the chip. We choose the distance to be 7cm where the field is around 25mT. Here, we also see how the simulation fits accurately with the theoretical prediction.

When rotating along the $\hat{\theta}$ direction in Fig. 11, we see two peak deviations at $\pi/2$ and $3\pi/2$. with peak value being $\sqrt{2}$ times higher than the minimum value. Since the chip is in $\hat{r} - \hat{\theta}$ plane, the deviation has contribution from both directions

$$d = ||\frac{3a}{r}\hat{\theta} - \frac{3a}{r}\hat{r}||_2 = \frac{3\sqrt{2}a}{r} \tag{12}$$

When rotating along the $\hat{\phi}$ direction in Fig. 12, since contributions are the same from $\hat{r}$ and $\hat{\theta}$, we see no deviation difference up to first order.

When rotating along the $\hat{r}$ direction in Fig. 13, the chip remain in $\hat{\theta} - \hat{\phi}$ plane. However rotating the square chip changes the maximum distance of the $\hat{\theta}$ direction as it vary from side length to diagonal length. Thus we see 4 peaks at $\pi/4, 3\pi/4, 5\pi/4, 7\pi/4$ with the peak $\sqrt{2}$ times bigger than the minimum deviation.

Therefore, different orientations of the chip will result in at most a factor of $\sqrt{2}$ difference for the deviation.
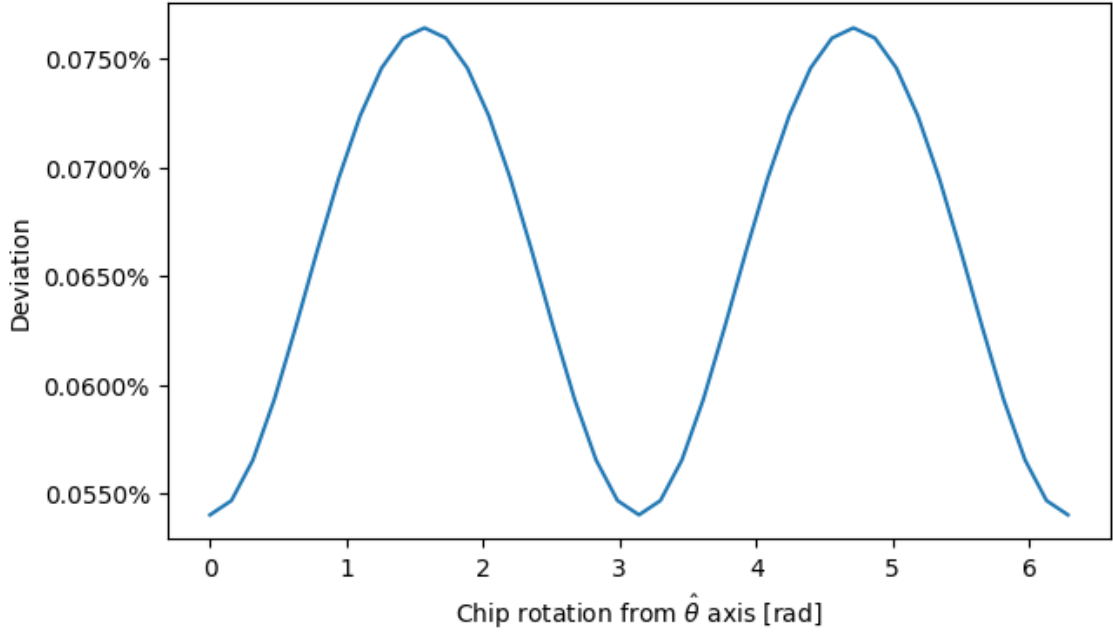

Figure 11: The deviation when chip is at different distances from the magnet.
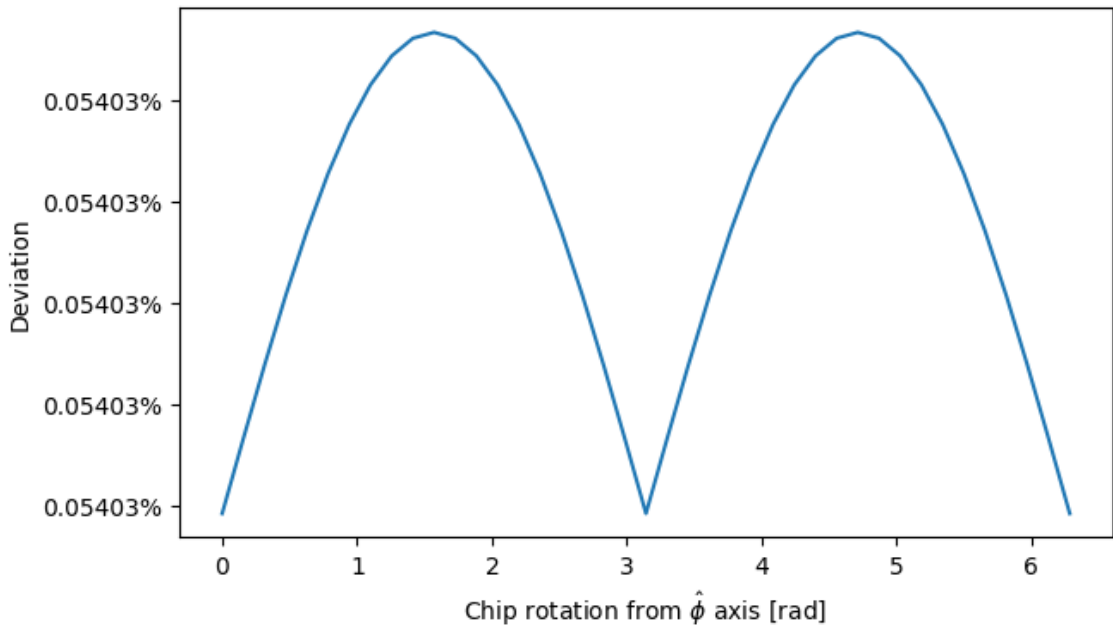

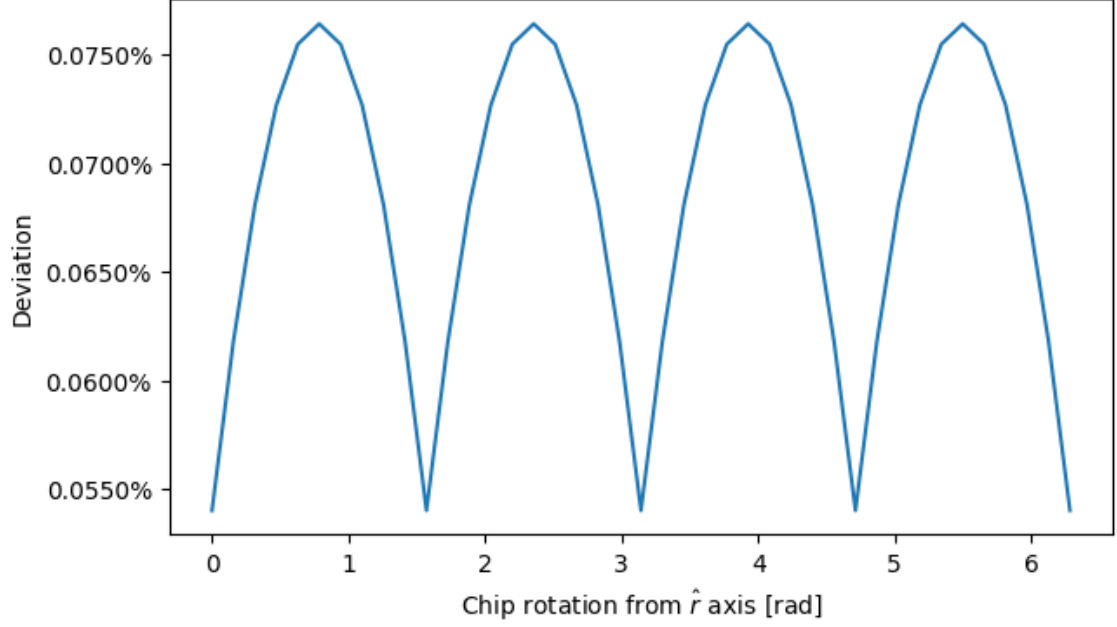Figure 12: The deviation when chip is at different distances from the magnet.

Figure 13: The deviation when chip is at different distances from the magnet.

4.3 Noise analysis

The next thing we want to estimate is the potential noise an external magnet can bring to the qubit. In previous work [9], the hysteresis effect is observed from the motor for magnet movement. This leads to approximately $50\mu m$ offset per start-and stop event for the movement of 1mm. However, this should not be considered as decohering noise since such an offset can be predicted/compensated. Also, such an offset only exists when we want to reposition the magnet and can be accurately measured when the magnet is still. The main noise comes from potential random vibration of the positioner, which is more prone to these disturbances since the magnet is no longer inside the concealed fridge.
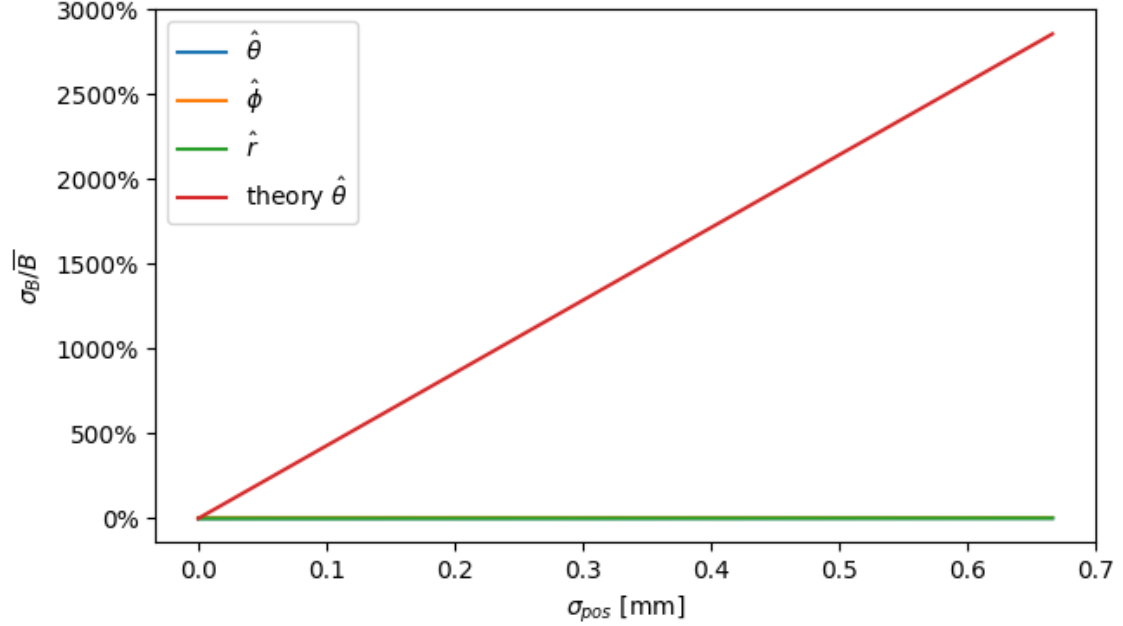

Figure 14: The deviation when chip is at different distances from the magnet. We also show the theoretical prediction of the dependency for $\hat{\theta}$ direction, which is in line with simulation result.

The Larmor frequency of quantum dot qubits usually ranges from a few hundred MHz to a few GHz. In comparison, the mechanical vibration of the positioner has a far lower frequency. Thus, we can model noise from the magnet as a quasistatic noise. Assuming that the offset amplitude of
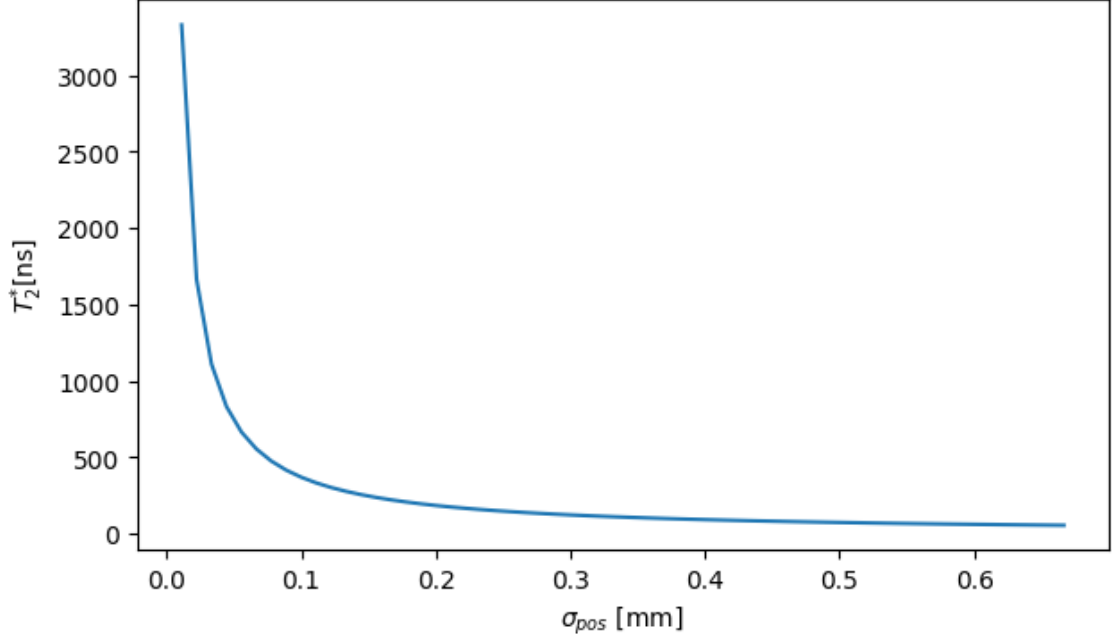
Figure 15: How T_2^* depend on the standard deviation of the magnet position.

the magnet follows a gaussian distribution that does not exceed 2mm, aka $3\sigma_{pos} < 2mm$. Since the fluctuations are small, the resulting magnetic deviation also follows a gaussian distribution, and the relation can be calculated using (10) in the same way we calculated the deviation in the previous section. From Fig. 14, we see that only vibration from the $\hat{r}, \hat{\theta}$ direction will cause magnetic field fluctuation. At the same time, only $\hat{r}$ direction vibration will have a magnetic field deviation in $\hat{\theta}$ direction – parallel to the magnetic field, which has a first order effect on the magnetic field amplitude. Since the larmor frequency is proportional to the field amplitude, the resulting Larmor frequency distribution becomes

$$P(\omega) = \frac{1}{\sqrt{2\pi}\sigma_\omega}e^{-\frac{(\omega-\omega_L)^2}{2\sigma_\omega^2}} \tag{13}$$

$$\sigma_\omega = \omega_L\frac{\sigma_B}{B} = \omega_L\frac{3\sigma_{pos,r}}{r} \tag{14}$$

For quasistatic noise, the coherence function is the Fourier transform of the noise distribution from which we can deduce T_2^* time:

$$f(t) = \langle S^+(t)\rangle = \langle S^+ \int_{-\infty}^{+\infty} P(\omega)e^{it\omega}d\omega\rangle \tag{15}$$

$$= \langle S^+ e^{i\omega_L t}e^{\frac{-\sigma_\omega^2 t^2}{2}}\rangle \tag{16}$$

$$= f(0)e^{i\omega_L t}e^{\frac{-\sigma_\omega^2 t^2}{2}} \tag{17}$$

$$= f(0)e^{i\omega_L t}e^{-\frac{1}{2}\left(\frac{t}{T_2^*}\right)^2}, \quad T_2^* = \frac{1}{\sigma_\omega} \tag{18}$$

We will thus have a gaussian decay for the qubit coherence with relaxation time T_2^* inverse to σ_ω. From Fig. 15, we can see the estimation of T_2^* time assuming the larmor frequency to be 1GHz. We can see that for strong vibration, the T_2^* is considerably affected. Although we can argue that such quasistatic noise can be largely cancelled by dynamical decoupling, we still see that such a positioner could be sensitive to mechanical vibration in certain cases.

In conclusion, the T_2^* is sensitive to vibration on the $\hat{r}$ direction and could affect the qubit performance when strong vibration exists. Given the setup in our positioner, this corresponds to vertical vibration of the magnet.

15

4.4 Data management

All CAD designs for the complete setup, along with the specific parts discussed in Chapter 3, and the simulation data outlined in this chapter with the associated code, are available in our GitHub repository [16].

5 Discussion

5.1 Reflection

The development of the magnet positioning system was not fully completed due to delays in the delivery of several critical manufactured components. These parts, mainly the X-plate and Z-plate which were essential for the mechanical assembly and calibration of the positioning mechanism, did not arrive in time to allow for integration and testing during the project period. As a result, key functionalities such as positional feedback verification and dynamic control tuning could not be carried out as planned.

The delay was mainly due to our reliance on external manufacturing and the lack of sufficient buffer time in the project schedule to account for possible production or shipping setbacks. Additionally, some design iterations were finalized later than expected, which further compressed the available window for ordering and assembly.

In retrospect, this issue could have been mitigated through earlier procurement planning and risk management. Placing the manufacturing orders sooner, or designing provisional substitute components for early-stage testing could have reduced dependency on external timelines. Improved communication with the manufacturer to track progress and confirm lead times would also have helped anticipate and respond to potential delays.

5.2 Success criteria evaluation

Even though we were not able to finalize the product, we were still able to achieve some intermediate progress. This progress will be assessed by evaluating our success criteria.

The project began with a set of predefined success criteria that guided the design and development of the magnet positioning system. In this section, we reflect on how these criteria were addressed and evaluate the corresponding outcomes.

- **Positioning Precision:** The motor control system was required to achieve a positioning accuracy of at least 0.1 mm in all three spatial axes to ensure magnetic field stability relative to the qubit's field sensitivity. Due to the incomplete assembly of the mechanical structure, this specification could only be experimentally verified in the x direction with the anti backlash nut. However, the same principle should apply for the y direction.

- **Magnetic Field Range and Control:** The system was designed to provide continuously adjustable magnetic fields up to 25 mT at the sample location. Based on measurements compared to simulation results and magnetic field calculations (described in section 4.1), we are confident that the current electromagnet configuration fulfills this requirement. The range of the magnet positioner in the Z-direction was designed with these specific requirements in mind.

- **Qubit Performance Preservation:** A key criterion was ensuring that the new magnet positioner maintains qubit dephasing times (T_2^*) comparable to those obtained using the existing superconducting solenoid. Since the physical assembly was not completed, this verification could not be performed. This assessment will ultimately depend on future testing conducted by the research group that integrates the system with their qubit setup. Instead, we estimated the T_2^* for the qubit with reasonable assumptions and simulation. It shows the T_2^* is sensitive to the vibration strength and it is only sensitive to vibrations perpendicular to the magnet. In our framework, this correspond to vertical vibration.

- **Gate Fidelity Maintenance:** Achieving single-qubit gate fidelities of at least 99.9% in benchmarking tests requires integration of the magnet system with the quantum hardware. As testing was contingent upon a completed setup, this requirement remains to be verified in collaboration with the end users during the next stage of project deployment.

- **Magnetic Field Mapping Capability:** Making use of a Hall sensor with associated evaluation software, we showed the capability to log and save the magnetic field measurements in a single direction. Furthermore, after some postprocessing we were able to visualize the field strength and compare it to our simulations which can be seen in Fig. 6. Hence, we believe that the full mapping of the magnetic field is also possible once the entire assembly is completed.

- **Structural Stability:** The structural design aims to minimize vibration-induced field fluctuations through high rigidity and reduced mechanical resonance. Although the final structure has not yet been assembled, material choices and design simulations indicate that the mechanical stability criterion is likely to be met once manufacturing and integration are completed.

In summary, the success criteria related to positioning precision, magnetic field range and mapping capability were partially achieved within the scope of the project. Criteria dependent on the physical assembly and integration, such as positioning precision, qubit performance preservation, gate fidelity maintenance, and structural stability, remain to be validated. Overall, the design phase established a strong foundation to meet all goals once the remaining components are delivered and assembled.

5.3 Future Plan of Attack

This section outlines a proposed plan for achieving and validating the success criteria that were not fully met during the initial project phase. Each subsection focuses on a specific criterium, detailing methods of assessment, potential challenges, and further steps to ensure successful realization.

5.3.1 Positioning Precision

To verify the required positioning accuracy of better than 0.1 mm in all three axes, precision calibration experiments will be conducted once the mechanical structure is assembled. The plan could include integrating high-resolution optical encoders or laser displacement sensors onto each axis to measure actual movement relative to commanded positions.

Evaluation will involve repeated motion sequences and comparison between commanded and measured displacements to determine both static and dynamic precision. If deviations exceed the tolerance, potential improvements include refining motor control parameters, improving the mounting rigidity, or looking into higher quality motors.

5.3.2 Qubit Performance Preservation

To assess the influence of the magnet positioner on qubit dephasing times (T_2^*), the system will be tested in conjunction with a qubit setup operated by the partner research group. The procedure involves performing Ramsey or spin echo experiments under various magnetic field configurations generated by the positioner. The resulting T_2^* values will be compared to baseline results obtained with the superconducting solenoid.

Should the T_2^* times degrade noticeably, the next step will be to identify possible noise sources introduced by the new system, such as current fluctuations, magnetic field instabilities, or mechanical vibrations. Adjusting current stabilization, improving shielding, or refining control electronics could be considered to mitigate these effects.

5.3.3 Gate Fidelity Maintenance

The goal of maintaining gate fidelities above 99.9% can be tested using randomized benchmarking experiments with the magnet positioner integrated into the quantum hardware setup. This approach quantifies the average error per gate under varying magnetic field conditions.

If the measured fidelities fall below the target value, diagnostic tests should be performed to identify whether the issue stems from magnetic field noise, cross-talk between control channels, or thermal effects induced by the magnet coils. Based on these findings, the control algorithms and magnetic stabilization methods can be optimized, or additional passive and active noise suppression techniques can be introduced.

5.3.4 Structural Stability

After assembly, the structural stability will be experimentally validated by measuring vibration spectra of the positioning system during operation. This can be achieved using accelerometers or laser vibrometers attached to key structural components. The amplitude and frequency of mechanical oscillations will be compared to the frequencies relevant to qubit sensitivity.

If significant vibration modes are detected near critical operating frequencies, reinforcement of the frame or damping materials can be introduced to shift resonances away from sensitive bands. Additionally, mechanical coupling between moving parts can be optimized to further minimize unwanted vibrations.

6 Interdisciplinarity and teamwork

In this section, the various scientific disciplines explored in this project are discussed, as well as the teamwork during the project.

6.1 Interdisciplinary aspects

The interdisciplinary aspects of the Magnet Positioner project are central to both the process and the solution, drawing on expertise and methodologies from physics, engineering, computer science, and system design.

The project leverages methods and knowledge from quantum physics to define the requirements for magnetic field alignment and qubit performance, as well as to interpret simulation results relating to magnetic noise and field homogeneity. Engineering design principles guide the development of hardware structures, including the selection of materials for rigidity, weight, and magnetic properties, and the mechanical design of the gantry frame and xyz-movement assembly. Computer science and automation are incorporated through the use of CAD modeling (Autodesk Inventor) for 3D simulation, control algorithms for the stepper motors (Arduino UNO interface), and data analysis software for magnetic field mapping and real-time monitoring.

The process brings together simulation-based analysis, mechanical design, electronic control, and risk management strategies. The solution's success criteria span quantitative (positioning accuracy, field range, gate fidelity) and qualitative (mechanical stability, safety protocols) metrics, requiring cross-disciplinary knowledge and skills.

6.2 Collaboration and team dynamics

At the start of the project, each member of the team already had some idea where there interests would lie within this project. As explained in the section above, the project consisted of various disciplines, where each member of the team felt slightly more comfortable to some disciplines than others. Given the various engineering aspects to this projects, each member of the team could start the project with a certain focus (e.g. figuring out the motors or starting with the CAD design). We would meet up often to show each other what we worked on, which made the start of the project very smooth. Moreover, all the team members were interested in all the aspects of the project, which meant that the team would have numerous useful discussions about what the next steps would be. This way of working persisted throughout the duration of the project and all team members are content with the way it went.

However, the project was not finished in time, which begs the question of how this came to be. The team suspects that this could have been avoided if the team was more conscious of the manufacturing times of the parts. Many critical parts are still not finished, which was the main reason this project could not be finished in time. Some delays were out of the control of the team, however this situation could have been avoided if the urgency had existed right at the start of the project. In hindsight, the team should have treated the manufacturing team with more urgency. Moreover, dummy parts could have been designed and manufactured to at least provide some clarity on some of the success criteria.

All in all, the team does feel that a lot has been accomplished during the duration of the project. This includes: a complete CAD design of the magnet positioner, motor testing with some of the

bigger and heavier parts, magnetic field simulations and software to map the magnetic field with a comparison to real measurements, albeit only in one direction. Even though the project was not completed as we envisioned it to be at the start, the team is confident that a future project team can build upon our results and finish the project as it was intended to be.

7   Acknowledgments

References

[1]   D. Loss and D. P. DiVincenzo, "Quantum computation with quantum dots," *Physical Review A*, vol. 57, no. 1, pp. 120–126, Jan. 1998, ISSN: 1094-1622. DOI: 10.1103/physreva.57.120. [Online]. Available: http://dx.doi.org/10.1103/PhysRevA.57.120.

[2]   G. Burkard, T. D. Ladd, A. Pan, J. M. Nichol, and J. R. Petta, "Semiconductor spin qubits," *Rev. Mod. Phys.*, vol. 95, p. 025 003, 2 Jun. 2023. DOI: 10.1103/RevModPhys.95.025003. [Online]. Available: https://link.aps.org/doi/10.1103/RevModPhys.95.025003.

[3]   L. M. K. Vandersypen et al., "Interfacing spin qubits in quantum dots and donors—hot, dense, and coherent," *npj Quantum Information*, vol. 3, no. 1, Sep. 2017, ISSN: 2056-6387. DOI: 10.1038/s41534-017-0038-y. [Online]. Available: http://dx.doi.org/10.1038/s41534-017-0038-y.

[4]   A. G. Fowler, M. Mariantoni, J. M. Martinis, and A. N. Cleland, "Surface codes: Towards practical large-scale quantum computation," *Physical Review A*, vol. 86, no. 3, Sep. 2012, ISSN: 1094-1622. DOI: 10.1103/physreva.86.032324. [Online]. Available: http://dx.doi.org/10.1103/PhysRevA.86.032324.

[5]   C. Gidney, "How to factor 2048 bit rsa integers with less than a million noisy qubits," 2025. arXiv: 2505.15917 [quant-ph]. [Online]. Available: https://arxiv.org/abs/2505.15917.

[6]   G. Scappucci et al., "The germanium quantum information route," *Nature Reviews Materials*, vol. 6, no. 10, pp. 926–943, Dec. 2020, ISSN: 2058-8437. DOI: 10.1038/s41578-020-00262-z. [Online]. Available: http://dx.doi.org/10.1038/s41578-020-00262-z.

[7]   V. John et al., "A two-dimensional 10-qubit array in germanium with robust and localised qubit control," 2025. arXiv: 2412.16044 [cond-mat.mes-hall]. [Online]. Available: https://arxiv.org/abs/2412.16044.

[8]   N. W. Hendrickx et al., "Sweet-spot operation of a germanium hole spin qubit with highly anisotropic noise sensitivity," *Nature Materials*, vol. 23, no. 7, pp. 920–927, May 2024, ISSN: 1476-4660. DOI: 10.1038/s41563-024-01857-5. [Online]. Available: http://dx.doi.org/10.1038/s41563-024-01857-5.

[9]   C. X. Yu et al., "Optimising germanium hole spin qubits with a room-temperature magnet," 2025. arXiv: 2507.03390 [quant-ph]. [Online]. Available: https://arxiv.org/abs/2507.03390.

[10] G. Da Prato, Y. Yu, R. Bode, and S. Gröblacher, "Step-by-step design guide of a cryogenic three-axis vector magnet," *Review of Scientific Instruments*, vol. 96, no. 6, Jun. 2025, ISSN: 1089-7623. DOI: 10.1063/5.0270187. [Online]. Available: http://dx.doi.org/10.1063/5.0270187.

[11] C. Adambukulam et al., "An ultra-stable 1.5 T permanent magnet assembly for qubit experiments at cryogenic temperatures," *Review of Scientific Instruments*, vol. 92, no. 8, 2021.

[12] *Proteox MX dilution refrigerator*, https://nanoscience.oxinst.com/products/proteoxmx, Accessed: 31-10-2025.

[13] M. Ortner and L. G. C. Bandeira, "Magpylib: A free python package for magnetic field computation," *SoftwareX*, vol. 11, p. 100 466, 2020.

[14] Michael-Ortner et al., *Magpylib*, version 5.2.1, Jun. 25, 2023. [Online]. Available: https://magpylib.readthedocs.io/en/latest/.

[15] C.-A. Wang et al., "Operating semiconductor quantum processors with hopping spins," *Science*, vol. 385, no. 6707, pp. 447–452, 2024. DOI: 10.1126/science.ado5915. eprint: https://www.science.org/doi/pdf/10.1126/science.ado5915. [Online]. Available: https://www.science.org/doi/abs/10.1126/science.ado5915.

[16] *Magnet-positioner-project*, https://github.com/iDragos1234/Magnet-Positioner-Project, GitHub repository., 2025.

A Maximum weight calculation of NEMA 17 stepper motors

Given that a single stepper motor has a maximum holding torque of $\tau = 0.55$ Nm and a lead screw radius of $r = 4$ mm, it easily follows from the torque formula

$$\tau = \mathbf{r} \times \mathbf{F}_E,$$

that the effort force is $F_E = 137.5$ N. The efficiency of the lead screw is given by

$$\eta = \frac{tan(\alpha)}{tan(\alpha + \beta)},$$

where α is the lead angle and β is the friction angle. Given that the lead screw has a pitch $P = 2$ mm and assuming the coefficient of friction between the rotating components is $f = 0.3$, we find $\alpha = tan^{-1}(\frac{P}{2\pi r}) \approx 4.550°$ and $\beta = tan^{-1}(f) \approx 16.699°$. Therefore the lead screw has an efficiency of $\eta \approx 20.4\%$.

Using this and the velocity ratio of the lead screw $VR = 2\pi r/P = 4\pi$, it follows that the mechanical advantage is $MA = VR \cdot \eta \approx 2.57$. Finally, the load force is given by

$$F_L = F_E \cdot MA$$

resulting in $F_L = 353.6$ N, or equivalently a weight of around 36 kg per motor.